PNAS RESEARCH ARTICLE | ENGINEERING

Self-powered, light-controlled, bioresorbable platforms for programmed drug delivery

Yamin Zhang[a,b], Fei Liu[a,b,c], Yuhe Zhang[a,b], Jin Wang[a,b,c], Dominic D'Andrea[d], Jordan B. Walters[d], Shupeng Li[e], Hong-Joon Yoon[a,b,f], Mingzheng Wu[a,b,g], Shuo Li[a,b], Ziying Hu[a,b], Tong Wang[h], Junhwan Choi[a,b,i], Keith Bailey[j], Elizabeth Dempsey[k], Kaiyu Zhao[a,b,c], Anastasia Lantsova[l], Yasmine Bouricha[d], Ivy Huang[a,b,c], Hexia Guo[a,b,c], Xinchen Ni[a,b], Yunyun Wu[a,b], Geumbee Lee[a,b], Fuchang Jiang[l], Yonggang Huang[e], Colin K. Franz[b,d,m,n,1], and John A. Rogers[a,b,c,e,o,1]

Edited by Samir Mitragotri, Harvard University, Cambridge, MA; received October 17, 2022; accepted February 6, 2023 by Editorial Board Member Evelyn L. Hu

Degradable polymer matrices and porous scaffolds provide powerful mechanisms for passive, sustained release of drugs relevant to the treatment of a broad range of diseases and conditions. Growing interest is in active control of pharmacokinetics tailored to the needs of the patient via programmable engineering platforms that include power sources, delivery mechanisms, communication hardware, and associated electronics, most typically in forms that require surgical extraction after a period of use. Here we report a light-controlled, self-powered technology that bypasses key disadvantages of these systems, in an overall design that is bioresorbable. Programmability relies on the use of an external light source to illuminate an implanted, wavelength-sensitive phototransistor to trigger a short circuit in an electrochemical cell structure that includes a metal gate valve as its anode. Consequent electrochemical corrosion eliminates the gate, thereby opening an underlying reservoir to release a dose of drugs by passive diffusion into surrounding tissue. A wavelength-division multiplexing strategy allows release to be programmed from any one or any arbitrary combination of a collection of reservoirs built into an integrated device. Studies of various bioresorbable electrode materials define the key considerations and guide optimized choices in designs. In vivo demonstrations of programmed release of lidocaine adjacent the sciatic nerves in rat models illustrate the functionality in the context of pain management, an essential aspect of patient care that could benefit from the results presented here.

bioresorbable | self-powered | battery | drug delivery | light-controlled

Significance

Polymer matrices and porous scaffolds enable passive, gradual release of drugs, with relevance to important clinical applications. Actively controlled systems represent an appealing alternative due to capabilities in user-defined programmability over the timing of discrete release events. Nevertheless, requirements for supporting power supplies and wireless electronics, together with the need to surgically extract devices after a period of use, represent disadvantages that limit broad adoption. This work addresses this opportunity through a self-powered, light-controlled, bioresorbable platform that bypasses the need for separate power supplies and enables natural dissolution and clearance from the body after treatment. This miniaturized and wirelessly programmed drug delivery device represents a significant advance over previously reported technologies, with potential for pharmacological treatment of a broad range of diseases.

Passive release of drugs loaded into polymer matrices (1–4) or porous scaffolds (5–8) addresses essential needs in patient care across a broad set of clinical applications. Implantable microfluidic systems that integrate actively controlled gate valves represent alternatives that are appealing because they enable user-defined, programmable control over the timing of release events. Such valves serve as the basis for fluid control in vivo, widely utilized for drug delivery applications (9–18) through triggering mechanisms that range from those based on magnetic fields (16, 19, 20) and photons (17) to thermal stimuli (13) and electrical currents (9, 10, 15, 21, 22). The first two approaches are attractive because of their simplicity, but they do not allow for independent control over individual gates in arrays. The other two techniques overcome this disadvantage, but their operation requires power supplied by standard batteries (9, 10, 23) or radiofrequency (RF) energy transfer (12, 15). These components and the associated control electronics (24) limit the ability to miniaturize these types of devices; they also add significant cost and complexity in engineering designs and in practical aspects of use. Furthermore, in all cases except one recently reported example (15), these hardware systems require surgical extraction after a period of use.

Here we address these shortcomings through the introduction of a self-powered gate valve mechanism that is controlled by illumination from an external light source, with capabilities for wavelength-division multiplexing across arrays (Fig. 1 *A* and *B*). The drug reservoir structure itself acts as a battery, to provide power needed to open the gate valves. In this way, the valves operate without the need for external sources of power, such that the sizes of the devices are limited only by the volumes of the drug reservoirs. Construction with bioresorbable materials (25–28) for reservoirs and nearly all other key components leads to natural dissolution and clearance from the body on timescales that match those of the treatment process (Fig. 1*C*), thereby eliminating the need for surgical removal. The following describes detailed studies of the key features of these systems, including 1) self-powered corrosion of the gate valves, 2) wavelength-selective, light-controlled activation of these corrosion processes, 3) programmable operation of devices that incorporate small arrays of valves and corresponding drug reservoirs, and 4) mechanisms of

The authors declare no competing interest.

This article is a PNAS Direct Submission. S.M. is a guest editor invited by the Editorial Board.

[1]To whom correspondence may be addressed. Email: cfranz@sralab.org or jrogers@northwestern.edu.

This article contains supporting information online at https://www.pnas.org/lookup/suppl/doi:10.1073/pnas.2217734120/-/DCSupplemental.

Published March 8, 2023.

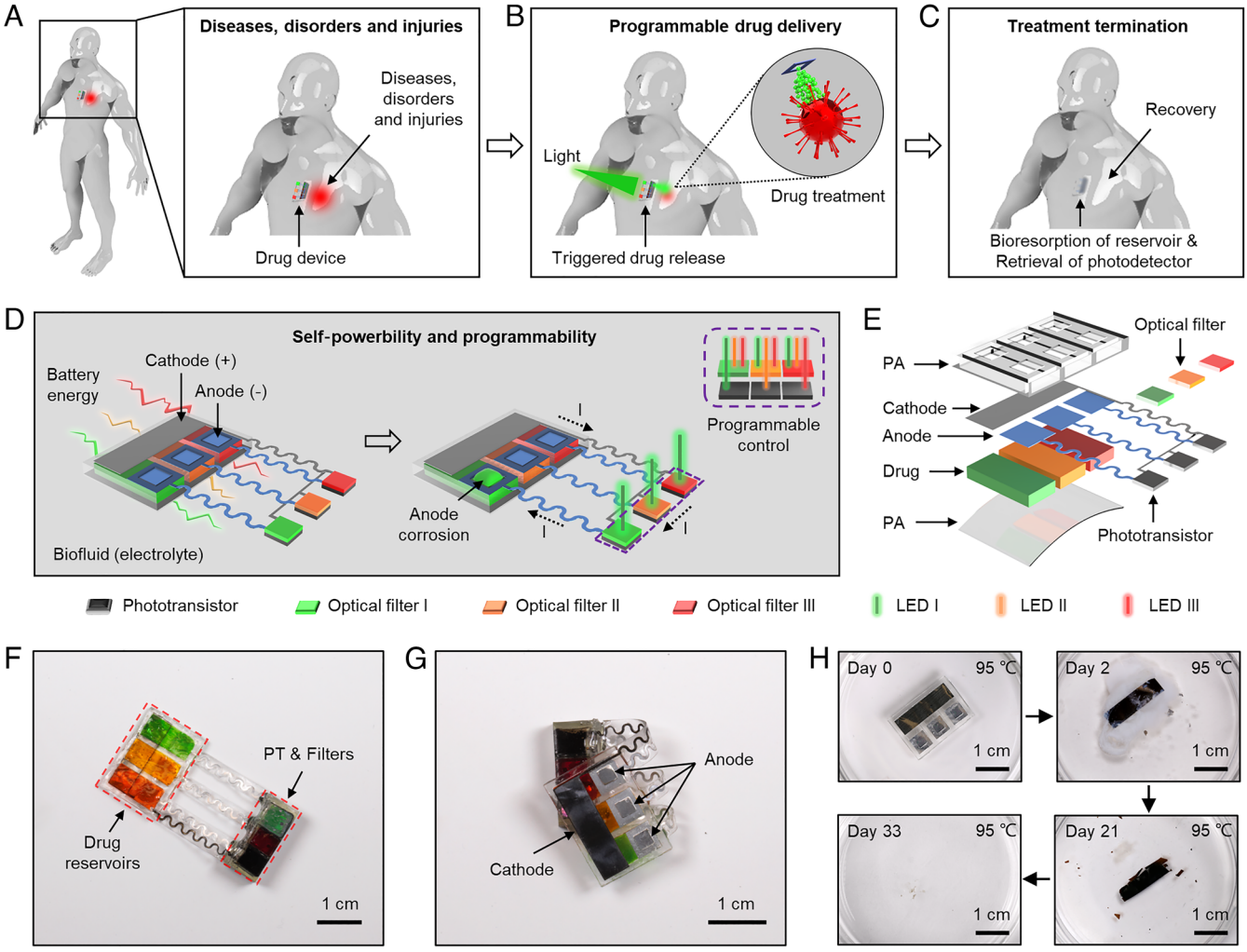

Fig. 1. Self-powered, light-controlled, bioresorbable devices for programmed drug release. Schematic illustrations of (*A*) the process for implanting a device at a site of interest, (*B*) the method for light-controlled, programmable release of drugs, (*C*) the mechanism of bioresorption after completion of the treatment. (*D*) Schematic diagrams of light-controlled opening of drug reservoirs by electrochemical corrosion of a metal gate structure that serves as the anode of a battery system, and as the basis for programmable release of drugs in an underlying reservoir. Illuminating the phototransistor decreases its electrical resistance and thus short circuits the electrochemical cell formed by the anode and cathode with surrounding biofluids as the electrolyte. This process initiates corrosion of the gate, and opening of the underlying drug reservoir. Optical filters placed atop the phototransistors create a wavelength selective response. Appropriate selection of LEDs and optical filters allows individual control of each reservoir. (*E*) Exploded view illustration of the device structure. (*F*) A device with a set of three bioresorbable drug reservoirs, connected to photodetectors through serpentine interconnects. (*G*) Drug reservoirs sealed with individual gates, which pair to one cathode. (*H*) Dissolution of a device without serpentine interconnects and phototransistors/filters, constructed from three 50-μm-thick Mg-SOG gates, a 5-μm-thick Mo cathode, and a reservoir structure and encapsulation of PA in PBS (pH 7.4) at 95 °C.

bioresorption for the constituent materials and sub-systems. Demonstrations of programmable pain control in rat models illustrate the capabilities and serve as the basis for investigations of biocompatibility and bioresorbability.

Results

Device Designs. Fig. 1*D* and *SI Appendix*, Fig. S1 summarize the mechanisms for self-powered operation and the scheme for remote, programmable control. In this example, a set of three electrochemically active, bioresorbable metal foils serves as a collection of isolated anodes. A foil of a more electropositive bioresorbable metal forms a counter electrode, as a single cathode. A molded structure of a bioresorbable polyanhydride (29) defines discrete reservoirs, each filled with a drug and sealed by an anode. Serpentine interconnects that extend from each anode connect to the emitter terminal of a corresponding phototransistor (PT) using a biodegradable conductive paste (Candelilla wax/W powder)(30). A separate serpentine interconnect joins the cathode to all of the collector terminals of the phototransistors. The interconnect structure allows drug reservoirs to be implanted to the sites of interest, including at depth below the surface of the skin, with phototransistors located at shallow locations below the skin, to facilitate illumination by an external light source. The implantation in the body forms a battery with a collection of electrochemical cells, one for each reservoir, where the biofluid serves as a common electrolyte. Exposing a phototransistor to light decreases its resistance and thus short circuits the corresponding cell. The result dramatically accelerates the corrosion of the anode, to open the underlying reservoir and allow release of drug into the surrounding tissues by passive diffusion. The device is self-powered because the drug reservoir structure itself acts as a battery, to provide power needed to open the gates. The phototransistor serves only as a passive switch, in the sense that exposure of this component of the system does not provide power for operating the device. Optical filters placed atop the phototransistors provide the basis for wavelength-selective activation. This scheme allows for independent control of each reservoir in the array, in a form of wavelength-division multiplexing. In the example

illustrated in Fig. 1, exposure to green, red, or infrared light from a light-emitting diode (LED), for example, selectively opens reservoir #1, #2, or #3, respectively, without opening the others. Multiple reservoirs can also be opened simultaneously in any combination by illumination with light of multiple colors. Supplementary Fig. 2 and *SI Appendix*, Table S1 summarize the advances of this technology approach over previously reported examples (9, 10, 12, 15, 23) that allow programmable control.

Fig. 1*E* shows an exploded view schematic illustration of the design. For cases reported here, the anode gates use Mg, Mg coated with spin-on-glass (Mg-SOG), or Zn. The cathodes use Fe, Mo, W, or MoO_3. Fig. 1 *F* and *G* and *SI Appendix*, Fig. S3 present photographs of a device with 5 mm × 5 mm Mg-SOG anodes (50 μm thick, 3 mm × 3 mm gate opening) and a 5 mm × 17 mm Fe cathode (25 μm thick). Each reservoir has dimensions of 5 mm × 13 mm and a depth of 1 mm, which corresponds to a drug volume of ~65 μL. The degradation rates of device materials can be affected by the pH, the presence of enzymes, and processes related to immune responses, as well as the temperature (*SI Appendix*, Table S2). The rates in all cases increase with temperature. The corrosion rates of Mg and Fe increase with decreasing pH (31, 32). By contrast, the degradation rates of Mo, SOG, and PA increase with increasing pH because OH^- initiates or facilitates the degradation reaction (29, 33, 34). Enzymes have minor or no impact on the degradation of Mg (35) and PA (36, 37). Fibrotic capsules that result from the immune response suppress the rate of corrosion of Mg (38) and may also decrease the degradation rates for other device components as a barrier to diffusive transport of biofluids and reaction products. Overall, the precise rate of degradation does not critically determine the utility of the device, as long as it disappears eventually, in a timeframe between a few months and a few years.

Fig. 1*H* and *SI Appendix*, Fig. S4 display results of accelerated aging tests that involve submerging a system without the interconnects and phototransistors/filters in phosphate-buffered saline (PBS) (pH 7.4) at 95 °C. Complete dissolution of 50-μm-thick Mg-SOG anodes, 250-μm-thick PA (1:1:2.5) encapsulation, and a 5-μm-thick Mo cathode occurs within 4, 17, and 33 d, respectively. The biodegradation mechanisms and rates of device materials, as well as their biological fates of the products of degradation, are summarized in *SI Appendix*, Fig. S5 and Tables S3 and S4. These data indicate that the device can be eliminated from the body (in vivo) after ~4 to 5 mo of implantation. The products of degradation of Mg, SOG, Mo, and PA are $Mg(OH)_2$, silicates, H_2MoO_4, and carboxylic acids, respectively. Each of these products is water soluble and is harmlessly excreted in the urine (26, 39–42). Fe degrades in a spatially nonuniform manner, with products (iron hydroxides) that have low solubility in biofluids but without known adverse biological effects (26). In this sense, Mo might be preferred to Fe for certain applications. H_2, as an additional degradation product of Mg, dissolves into the adjacent tissues, diffuses through these tissues and blood vessels, and can pass through the skin (43). Certain of these materials including Mg and PA are widely used in biodegradable, nonelectronic implants at significantly larger amounts, as further evidence of an understanding of their biocompatibility.

Choice of Gate and Battery Materials. Fig. 2*A* lists materials options for the bioresorbable electrodes, along with their main reactions with surrounding biofluids and standard electrochemical potentials. As mentioned above, the anodes include Mg or Zn, paired with cathodes of Fe, Mo, W, or MoO_3. The corresponding reactions that govern bioresorption in an aqueous environment

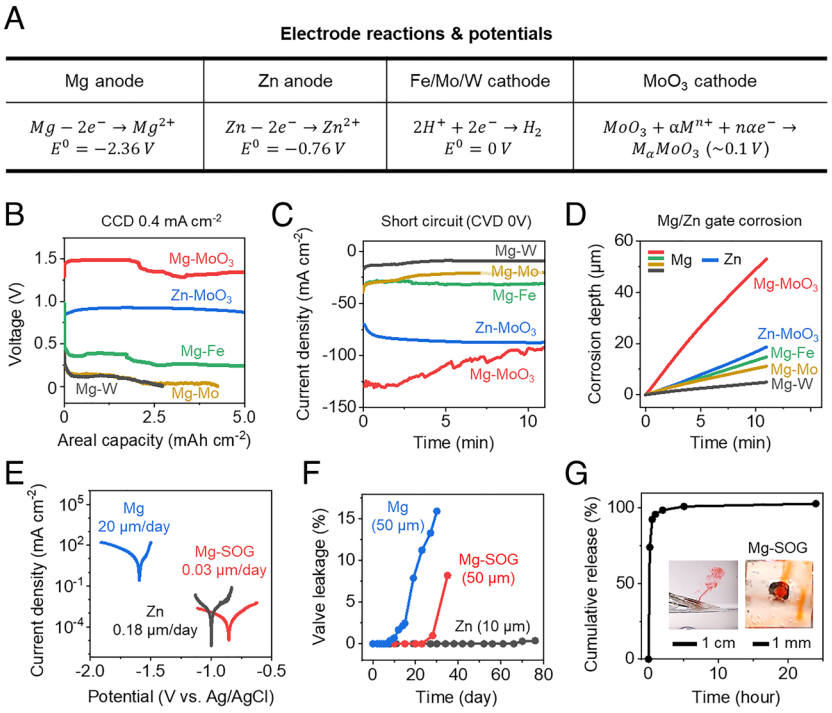

Fig. 2. Characteristics of bioresorbable gates and battery materials. (*A*) Electrochemical reactions and standard potentials of bioresorbable anodes (Mg, Zn, gate materials) and cathodes (Fe, Mo, W, MoO_3, counter electrodes for gates). (*B*) Voltage profiles of Mg-MoO_3, Zn-MoO_3, Mg-Fe, Mg-Mo, and Mg-W cells when discharged at a constant current density of 0.4 mA cm^{-2}. (*C*) Short-circuit current densities of Mg-MoO_3, Zn-MoO_3, Mg-Fe, Mg-Mo, and Mg-W cells. For a specific gate material (Mg or Zn foils), a high discharge rate indicates a high rate of gate corrosion and a correspondingly short gate triggering period. (*D*) Corrosion depth of Mg gates (paired with MoO_3, Fe, Mo, and W cathodes) and Zn gates (paired with MoO_3 cathodes) under a short-circuit condition. (*E*) Tafel plots of Mg, Mg-SOG, and Zn foils. The SOG coating greatly reduces the corrosion rate of the pure Mg. (*F*) Natural drug leakage from Mg, Mg-SOG, and Zn gates incubated in 37 °C PBS. Selection of gate materials determines the functional lifetime of the device. (*G*) Cumulative release of drug after opening the gate. The release of drug reaches 90% in 30 min, 95% in 1 h, and 99% in 2 h. Gate: Mg-SOG. Cathode: Fe. Photos: drug release into PBS (*Left*); opened Mg-SOG gate (*Right*).

are: $Mg + 2H_2O \rightarrow Mg(OH)_2 + H_2$; $Zn + 2H_2O \rightarrow Zn(OH)_2 + H_2$; $4Fe + 6H_2O + 3O_2 \rightarrow 4Fe(OH)_3$; $2Mo + 2H_2O + 3O_2 \rightarrow 2H_2MoO_4$; $2W + 2H_2O + 3O_2 \rightarrow 2H_2WO_4$. As reported in in vivo and in vitro studies of other types of bioresorbable electronic devices, these electrode materials harmlessly degrade and eventually disappear completely.(26, 27) Patterning of the electrodes (Mg, Zn, Fe, Mo, W) relies on a laser cutting process applied to metal foils. The MoO_3 cathodes result from casting of slurries of MoO_3 on laser-cut Mo foils. Discharging bioresorbable batteries formed with these electrodes by immersing them in PBS reveals their behaviors. As shown in Fig. 2*B* and *SI Appendix*, Fig. S6, Mg-MoO_3, Zn-MoO_3, Mg-Fe, Mg-Mo, and Mg-W cells generate an average voltage output of ~1.48 V, ~0.90 V, ~0.38 V, ~0.15 V, and ~0.13 V, respectively, and with an areal capacity in the range of 0 to 1.5 mAh cm^{-2}, when discharged at a constant current density (CCD) of 0.4 mA cm^{-2}. Due to the relatively high electropositivity of Zn, the devices formed with Zn-Fe, Zn-Mo, and Zn-W pairs show voltage outputs of ~0 V. These combinations are not considered further. Performing a short-circuit discharge at a constant voltage (CVD) of 0 V represents the self-powered operation scenario that follows from exposure of the phototransistors to light (Fig. 2*C*). The Mg-MoO_3, Zn-MoO_3, Mg-Fe, Mg-Mo, and Mg-W cells offer an average short-circuit current of 93, 85, 31, 24, and 10 mA cm^{-2}, respectively. For a specific metal anode (Mg or Zn), a high rate of discharge corresponds to a fast rate of gate corrosion and therefore a short triggering period for drug release. The Mg gate corrodes at an average rate of ~4.8, ~1.3, ~1.0, and ~0.4 μm/min when paired with MoO_3, Fe, Mo, and W cathodes, respectively. The Zn gate corrodes at an average rate of ~1.7 μm/min in a Zn-MoO_3 cell setup (Fig. 2*D*). *SI Appendix*, Fig. S7 and Note 1 present calculations of the capacity required for complete corrosion of the Mg and Zn gates. Increasing the size of the cathode enhances the rate of gate corrosion (*SI Appendix*, Fig. S8 *A* and *B*), thereby justifying the use of the large cathode in the device designs presented here. Four tests of the short-circuit process using the same Fe cathode and fresh Mg anodes reveal negligible differences in the current densities. This result confirms the ability of the Fe cathode to support at least three consecutive drug-release events (*SI Appendix*, Fig. S8*C*).

Mg, as the most electroactive bioresorbable metal, degrades at a rate of as high as ~1.2 to 12 μm/d in simulated body fluids and at physiological conditions (26). This timescale limits the lifetimes of devices that use Mg gates. Forming a coating of a polysiloxane-based spin-on-glass dielectric material (SOG, ~500 nm thickness) on the Mg foils enhances their stability in biofluids (44). This type of SOG is biocompatible and bioresorbable, as reported elsewhere (45). As determined by X-ray photoelectron spectroscopy, the chemical formula is $SiO_{1.8}C_{0.6}$ (*SI Appendix*, Fig. S9 *A* and *B*). The CH_3, Si-CH_3, and Si-O-Si bonds (46–49) identified by Fourier transform infrared spectroscopy are consistent with a silicon oxycarbide structure (*SI Appendix*, Fig. S9*C*). Scanning electron microscopy (SEM) shows a representative uniform coating of SOG on a Mg foil (*SI Appendix*, Fig. S9*D*). SOG dissolves at a rate of ~1 nm/d in 37 °C PBS (*SI Appendix*, Fig. S10). Performing linear sweep voltammetry (LSV) measurements through a three-electrode setup in PBS with Mg, Mg-SOG, or Zn as the working electrode, a Pt wire as the counter electrode, and Ag/AgCl as the reference electrode, indicates that the natural corrosion rates of Mg, Mg-SOG, and Zn are 20, 0.03, and 0.18 μm/d, respectively (Fig. 2*E*). The SOG coating greatly reduces the rate of the pure Mg metal, as expected. Coatings of SiO_2 (100 nm or 1 μm thick) formed by sputter deposition (Mg-SiO_2) also reduce the rates, but by a comparatively lesser extent, possibly due to defects in the SiO_2 as indicated in SEM images (*SI Appendix*, Fig. S11). Additional short-circuit discharge tests of cells with Mg-SOG or Mg-SiO_2 anodes and a Fe cathode confirm the ability of these anodes to function as gates. The case of Mg-SiO_2 shows similar discharge profiles to those with pure Mg, due to limited protection provided by the sputtered SiO_2. The Mg-SOG system behaves differently, however, with a low initial short-circuit current of <2 mA cm^{-2} and a gradual increase to 15 mA cm^{-2}, equivalent to the case of pure Mg, within 30 s (*SI Appendix*, Fig. S12*A*). Electrochemical impedance spectroscopy (EIS) measurements conducted through a three-electrode setup in PBS with Mg-SOG as the working electrode, a Pt wire as the counter electrode, and Ag/AgCl as the reference electrode provide some insights. EIS measured before and after short-circuiting electrochemical cells with Mg-SOG anodes and Fe cathodes (*SI Appendix*, Fig. S12*B*) show that the resistance of the SOG coating, more specifically the resistance of the defects (50), decreases from 1.2×10^6 to 2.8×10^4 ohm within 5 s after short-circuiting. Optical microscopy shows that this short-circuit discharge quickly destroys the SOG coatings as a result of pinholes that give rise to hydrogen bubbles generated from the corrosion reactions of the underlying Mg. These phenomena explain how the Mg-SOG gate corrosion can be triggered within a few seconds after activation in a short-circuit condition (*SI Appendix*, Fig. S12*C*). Corrosion rates of Mg-SOG recorded after its incubation in 37 °C PBS (*SI Appendix*, Fig. S13) provide data on the long-term protective ability of the SOG on Mg. Results show that the corrosion rate increases from 0.03 μm/d at day 0, to 0.2 and 1.4 μm/d at day 1 and day 17, respectively, likely due to pinholes in the SOG coating. The protection provided by the SOG thus extends the lifetime of 50-μm-thick Mg gates from 7 to 23 d (Fig. 2*F*), as confirmed by recording the leakage of water with dye (Rhodamine B) loaded into reservoirs sealed with Mg and Mg-SOG gates at 37 °C in PBS, as measured by ultraviolet–visible (UV–VIS) spectroscopy. Zn gates (10 μm) exhibit lifetimes of ~66 d, consistent with their natural rates of corrosion (0.18 μm/d, Fig. 2*E*). Triggering a drug release device formed with a 20-μm-thick Mg-SOG gate paired with a Fe cathode for ~10 min opens (defined as >1% drug release) the gate. The cumulative release of drug reaches 90% in 30 min, 95% in 1 h, and 99% in 2 h (Fig. 2*G*).

Programmability of the Drug Delivery Device. As described previously, programmability relies on a combination of phototransistors/filters and light sources with narrow spectral emission aligned with the transmission properties of the filters, in a form of wavelength-division multiplexing. Descriptions of specific choices for demonstrations reported here appear in *SI Appendix*, *Supplementary Note 2* and Fig. S14. The attenuation of light from LEDs at different implantation depths are calculated through a simplified Beer–Lambert law (51–53) (*SI Appendix*, Fig. S15). Light emitted from LED X selectively passes through optical filters X, illuminates phototransistor X, and triggers corrosion of Gate X (X = I, II, or III). In this sense, LED X, phototransistor X, Filter X, and Gate X form a matched group. The type of phototransistor used in this work has a dark current of 50 nA, corresponding to an "off" state resistance of 2 Mohms. This resistance decreases sharply upon increasing illumination, until reaching saturation at resistances of ~174, ~172, and ~91 ohms for illumination intensities of ~27, ~15, and ~64 mW cm^{-2}, by light from LEDs I, II, and III, respectively. The rate of gate corrosion depends on both the resistance of the phototransistor and the resistance of the electrochemical cell. The ideal scenario involves illumination from LED X at an "on" state intensity sufficiently high such that the resistance of the phototransistor X is much lower than that of the cell (~1 kohms), but sufficiently

low to avoid crosstalk between other phototransistor/filter sets. For the system reported here, the intensities from light emitted by LEDs I, II, and III at the location of the phototransistor/filter sets are below 10, 10, and 2 mW cm^{-2}, respectively, to ensure reliable programmability. As shown in *SI Appendix*, Fig. S16 *A* and *B*, the resistances of phototransistors underneath the matched filters are 62, 36, and 33 times smaller than that underneath the unmatched ones, for illumination by light from LEDs I, II, and III, respectively. For a three-reservoir drug device with Mg gates paired with a Fe cathode (Fig. 3*A*), the short-circuit current for the gate that connects to the phototransistor underneath the matched filter is > 25, > 11, and > 7 times that of the unmatched ones, for illumination by light from LEDs I, II, and III, respectively, which eliminates unwanted drug leakage from unmatched reservoirs, and ensures reliable programmability of release (*SI Appendix*, Fig. S16 *C–E*). As described before, a high short-circuit current corresponds to a fast gate-opening process. Finite element analysis (FEA, Fig. 3*B*) shows the current distributions of gates under 10, 10, and 2 mW cm^{-2} light emitted from LEDs I, II, and III, respectively. Results indicate crevice corrosion processes, where the edges of the gates exhibit the highest corrosion rates, consistent with previous reports (15, 54). Fig. 3*C* presents a demonstration of programmable drug release, triggered by illuminating LEDs I, II, and III sequentially.

In Vivo Drug Delivery and Biocompatibility. Analgesic medications relieve pain from injuries due to trauma or medical procedures. A drug release device of the type introduced here can support programmable blocking of pain signals (Fig. 4 *A* and *B*), where the device ultimately dissolves in the body to avoid the need for surgical extraction after a period of use (Fig. 4*C*). Fig. 4*D* illustrates implantation with the gates placed adjacent to the sciatic nerve of a rat model. The reservoirs in this case contain lidocaine for local pain block through preferential binding to the inactivated state of the voltage-gated sodium channels (55). Fig. 4*E* presents a photograph that shows the site for implantation. The operation of three LEDs triggers programmable release of lidocaine from one or multiple reservoirs. Compound muscle action potentials (CMAPs) and sensory nerve action potentials (SNAPs) measured before and after release quantify the efficacy of nerve block (Fig. 4 *F* and *G*). The release from a single reservoir leads to decreases in the amplitude of CMAP and SNAP by ~48% and ~55%, respectively. Releasing drugs from three reservoirs decrease the CMAP and SNAP amplitudes by ~87% and ~86%, respectively. The maximum block occurs within 15 min after release and nerve activity gradually recovers over the next ~1 h (*SI Appendix*, Fig. S17). To confirm the physiological effect of the lidocaine being released from the device, we measured the grip strength and Von Frey paw withdrawal threshold of both hindlimbs (Fig. 4 *H* and *I* and *SI Appendix*, Fig. S18) before device implantation (baseline), after waking up from lidocaine release to the right sciatic nerves of rats (drug), and after 24 h recovery (recovery). The release of lidocaine to the right sciatic nerve induces a decrease in grip strength and an increase in paw withdrawal threshold of the right hindlimb, which confirmed the physiological effect of the lidocaine being released from the device. The grip strength and paw withdrawal threshold of the left (contralateral) hindlimb were measured as well to verify that the rats woke up completely from

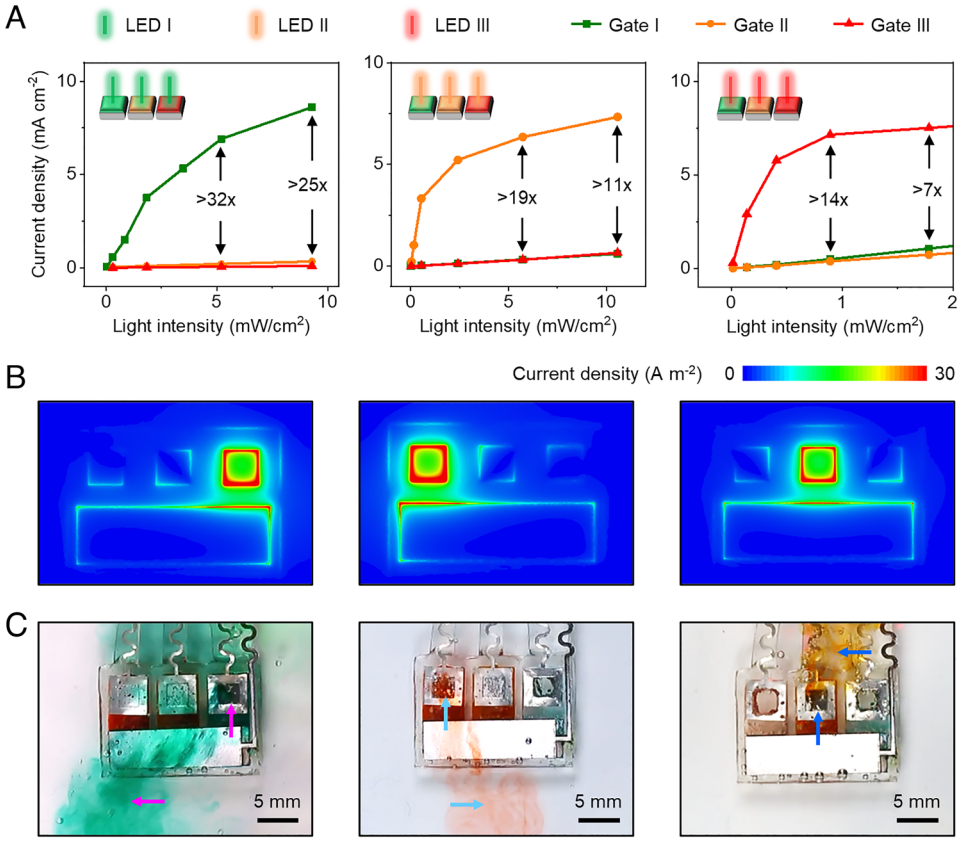

Fig. 3. Programmability via a light-controlled mechanism. (*A*) Simultaneous short-circuit current densities of all Mg gates (I, II, and III) paired with a Fe cathode, under different light intensities emitted from LED I, II, or III. x: ratio of short-circuit current between the matched and unmatched gates. This effective wavelength selection eliminates unwanted drug leakage from unmatched reservoirs, for reliable programmability. (*B*) FEA results for the current density distribution of each gate under illumination of LED I, II, or III, indicating crevice corrosion. (*C*) Programmable drug release events triggered by illuminating LEDs I, II, and III sequentially.

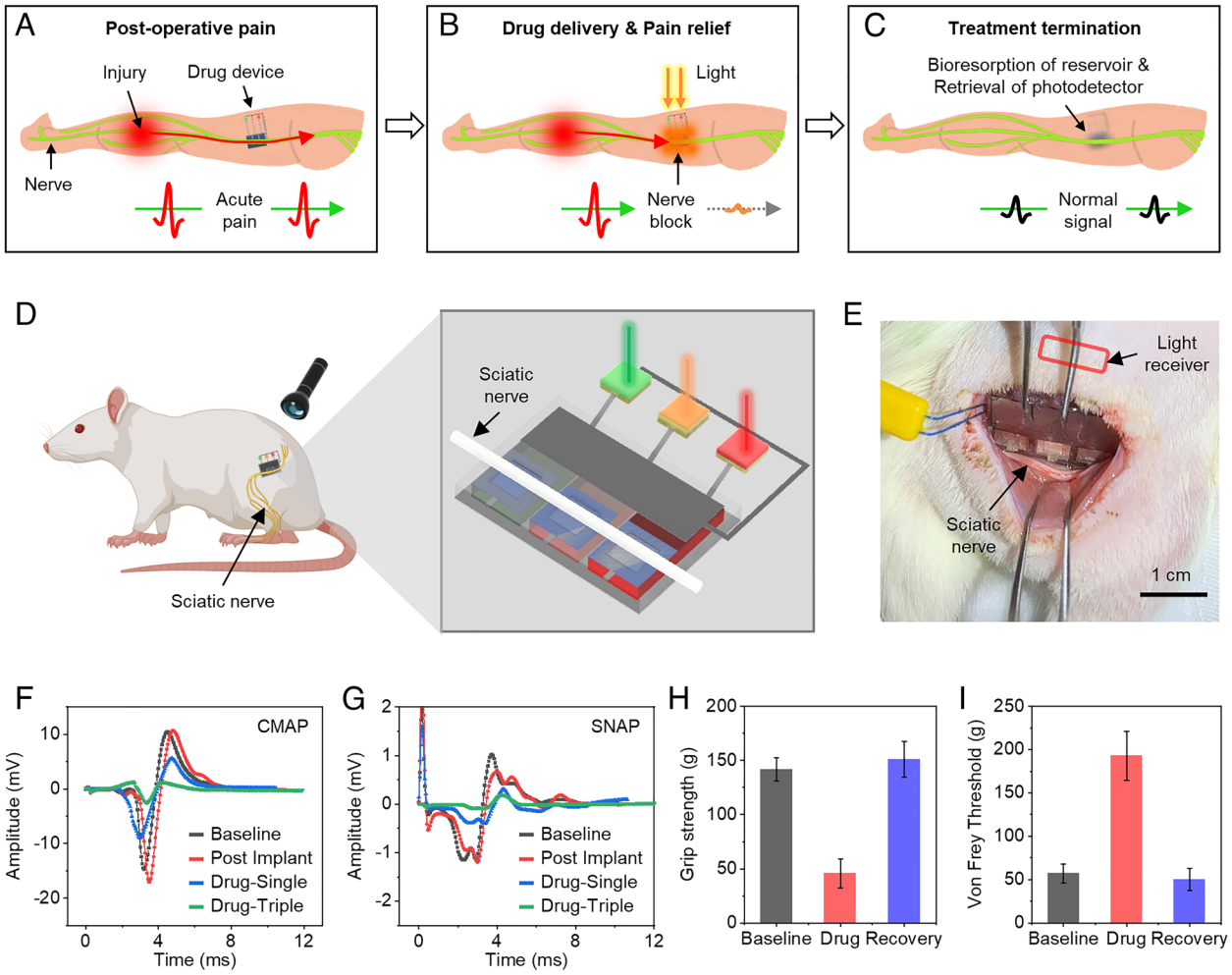

Fig. 4. In vivo studies of programmed release of lidocaine adjacent the sciatic nerves in rat models. Schematic illustrations of *A*, implantation of the drug device adjacent to the injured nerve, *B*, light-triggered drug release for programmable pain relief, *C*, bioresorption after treatment. (*D*) Illustration of the placement of a device with gates adjacent to the sciatic nerve of a rat. (*E*) Image of an implanted device. (*F* and *G*) Changes in CMAP (*F*) and SNAP (*G*) associated with programmable release of lidocaine from one (Drug-Single) or three (Drug-Triple) reservoirs by programmed control of LEDs. n = 3 biologically independent animals. Baseline is from healthy rats with no implants. (*H* and *I*) Measurements of the grip strength (*H*) and Von Frey paw withdrawal threshold (*I*) of right hindlimbs before device implantation (Baseline), after waking up from lidocaine release to the right sciatic nerves of rats (Drug), and after 24 h recovery (Recovery). n = 4 biologically independent animals.

general anesthesia. In this manner, the device can be utilized for programmed, on-demand pain relief during and after recovery from an injury or a surgical operation.

In vitro cytocompatibility studies of the device against human cells used both direct and indirect contact methods.The results indicate cytocompatibility of the device (*SI Appendix*, Fig. S19). Further evaluation of the biocompatibility of the gates and the devices involves subdermal implantation for 1-mo of a control group [PA (29), n = 4], a gate group (a Mg-SOG foil on PA, n = 4), and a device group (Mg-SOG and Fe foils on PA, n = 4), in the interscapular region of mice. The results in Fig. 5 *A* and *B* show negligible differences in the overall weight and changes in the weights of organ in mice throughout the gate, device, and control groups. Organs (brain, heart, lung, liver, spleen, and kidney) collected at 1- and 4-wk endpoints yields information on the biodistribution of key bioresorbable elements (Mg, Si, and Fe). Fig. 5*C* shows concentrations of Mg, Si, and Fe in organ tissues, measured by inductively coupled plasma optical emission spectrometry (ICP-OES). Device and gate groups show no abnormal accumulation of dissolved Mg, Si, and Fe in organ tissues compared to control group (*SI Appendix*, Tables S5 and S6 for analysis). *SI Appendix*, *Supplementary Note 4* discussed the possible reasons (56–58) for elemental changes in spleen (for Si, Fe, *SI Appendix*, Fig. S20) and heart (for Si), from 1-wk to 4-wk endpoints. The analysis of complete blood counts and blood chemistry tests reveal no statistically significant differences among control, gate, and device groups (significance level $P < 0.05$, One-Way ANOVA), suggesting no device-related organ toxicity or disruption of electrolytes (chloride, Cl; sodium, Na; bicarbonate, TCO2; phosphorus, PHOS; calcium, Ca; potassium, K) and enzymes (aspartate transaminase, AST; alkaline phosphatase, ALP; both are indicators for liver function) (Fig. 5*D*). The blood urea nitrogen values increased from ~19.7 mg/dL at 1 wk to ~28.2 mg/dL at 4 wk, which falls within the normal range of mice (18 to 29 mg/dL)(59) and might be attributed to the normal biological variability. Hematoxylin and eosin (H&E) images of stained tissue sections collected appear in Fig. 6 *A* and *B* and *SI Appendix*, Fig. S21, which indicates no damage to organ, skin, and muscle tissues and minimal to mild inflammatory cells related to implantation, consisting of loosely arranged histiocytes, neutrophils, and fibroblasts. At the end of 1 wk, small numbers of fibroblasts are present, indicating an early reparative process. At the end of 4 wk, the fibroblasts are more organized and

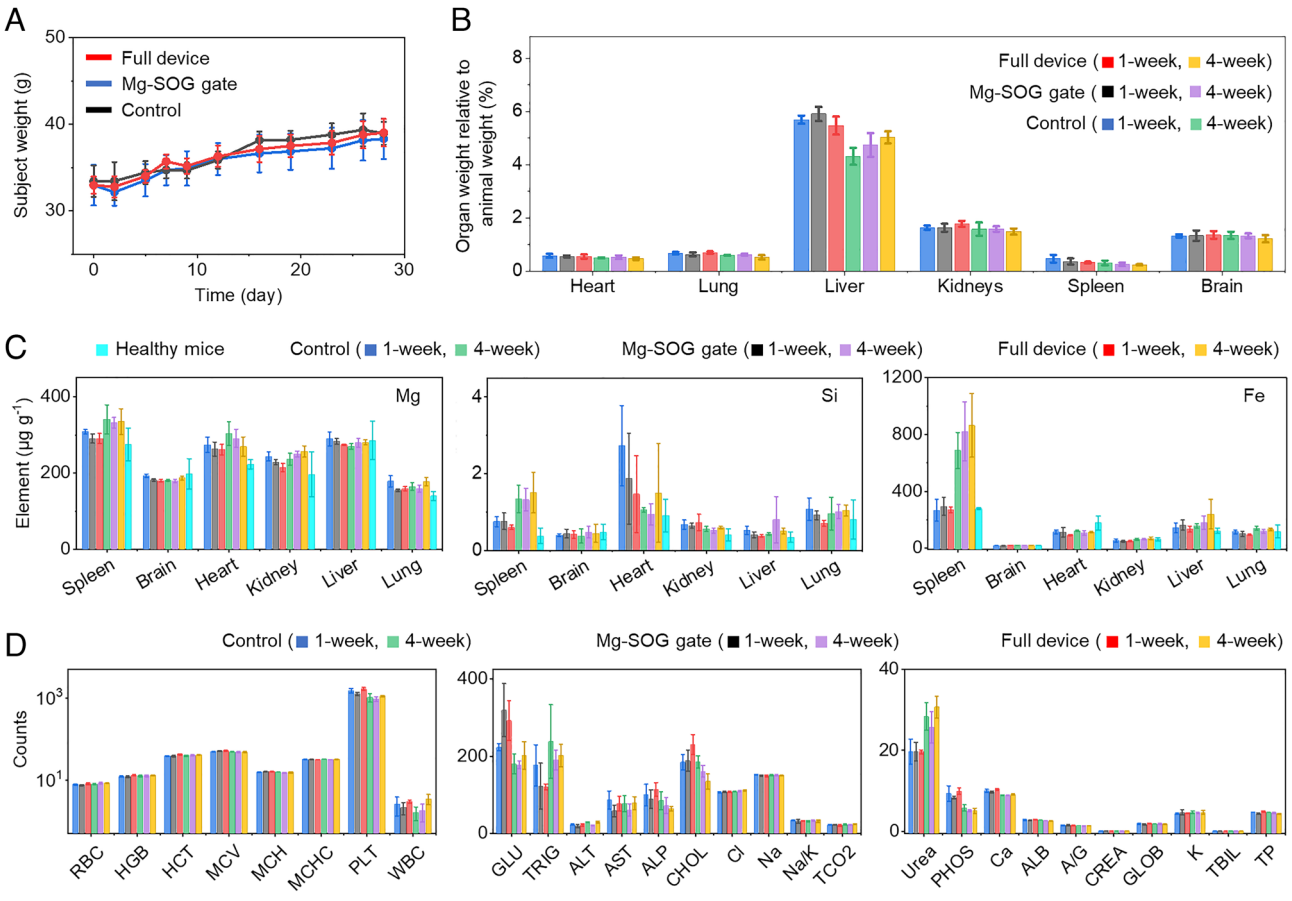

Fig. 5. In vivo biocompatibility and toxicity studies of Mg-SOG gates and full devices. (*A*) Change in the weight of mice following implantation. (*B*) Change of organ weight relative to animal weight after implantation at 1-wk and 4-wk endpoints. (*C*) In vivo biodistribution of key elements (Mg, Si, Fe) in organs. The elemental concentrations of Mg, Si, and Fe for healthy mice are obtained from previous reports (61–63). (*D*) Analysis of complete blood counts and blood chemistry. RBC, red blood cell (×1,000,000 μL^{-1}); HGB, blood hemoglobin level (g dL^{-1}); HCT, hematocrit level (%); MCV, mean corpuscular volume (fl); MCH, mean corpuscular hemoglobin (pg); MCHC, mean corpuscular hemoglobin concentration (g dL^{-1}); PLT, platelet count in blood (×1,000 μL^{-1}); WBC, white blood cell (×1,000 μL^{-1}); GLU, glucose (mg dL^{-1}); TRIG, triglycerides (mg dL^{-1}); ALT, alanine aminotransferase (U L^{-1}); AST, aspartate transaminase (U L^{-1}); ALP, alkaline phosphatase (U L^{-1}); CHOL, cholesterol (mg dL^{-1}); Cl, chloride (mmol L^{-1}); Na, sodium (mmol L^{-1}); Na/K, sodium/potassium ratio; TCO2, bicarbonate (mmol L^{-1}); Urea, blood urea nitrogen (mg dL^{-1}); PHOS, phosphorus (mg dL^{-1}); Ca, calcium (mg dL^{-1}); ALB, albumin (g dL^{-1}); A/G, albumin/globulin; CREA, creatinine (mg dL^{-1}); GLOB, globulin (g dL^{-1}); K, potassium (mmol L^{-1}); TBIL, total bilirubin (mg dL^{-1}); TP, total protein (g dL^{-1}). (*A–D*) Data are presented with error bars as means ± SD n = 4 biologically independent animals.

accompanied by deposits of loose fibrous tissue, consistent with a more organized inflammatory and reparative response to the implanted device. Dense fibrous capsule do not appear in any of the animals, suggesting a low severity of the inflammation and the absence of a robust immunologic response directed against the implanted device. This foreign body response might affect drug delivery process, which could be mitigated through pharmacological strategies [e.g., inflammasome inhibitor (60)]. Careful examination of H&E slides for fibrosis and inflammation in a five-grade scoring system (*SI Appendix*, Figs. S22 and S23) confirms the biocompatibility of the constituent materials used in this platform, consistent with previous reports (26, 27, 45). Additional biocompatibility studies involve triggering short-circuit of the device, a process that evolves hydrogen. Results (*SI Appendix*, Fig. S24) indicate that the device with hydrogen evolution during a short triggering period (~10 min) does not elicit a strong immune response and does not result in the presence of a dense fibrous capsule. Gas cavities are not present when removing devices at 1- and 4-wk endpoints, which could be attributed to hydrogen escape through dissolution into the adjacent tissues, diffusion into tissues and blood vessels, and excretion through skin (40, 43). Detailed calculations are in *SI Appendix*, *Supplementary Note 3*.

Discussion

This paper introduces a self-powered, light-controlled gate valve mechanism inspired by battery short-circuit phenomena and associated corrosion chemistry. A miniaturized drug delivery device built with bioresorbable materials in a multiple reservoir geometry serves as a demonstration vehicle for programmable operation. Here, phototransistors with integrated optical filters act as optically controlled switching elements to activate corresponding gates by illumination with light-emitting diodes. Animal model experiments illustrate the use of this system for on-demand pain relief and provide data on the aspects related to biocompatibility and bioresorbability. The limitations of this work include 1) the use of non-resorbable phototransistors and optical filters and 2) the practical constraints on the number of reservoirs that can be independently addressed using our optical strategy. On-going research focuses on designs for resorbable components to address the first limitation (61). For the second, given angular uncertainties and optical scattering by biological tissues, optical filters with transmission bandwidths less than ~20 nm (64) will be ineffective. Considering a realistic range of wavelengths based on tissue absorption and subdermal location of photodetectors of the system, i.e., 400 nm to 1,000 nm, this transmission bandwidth limitation

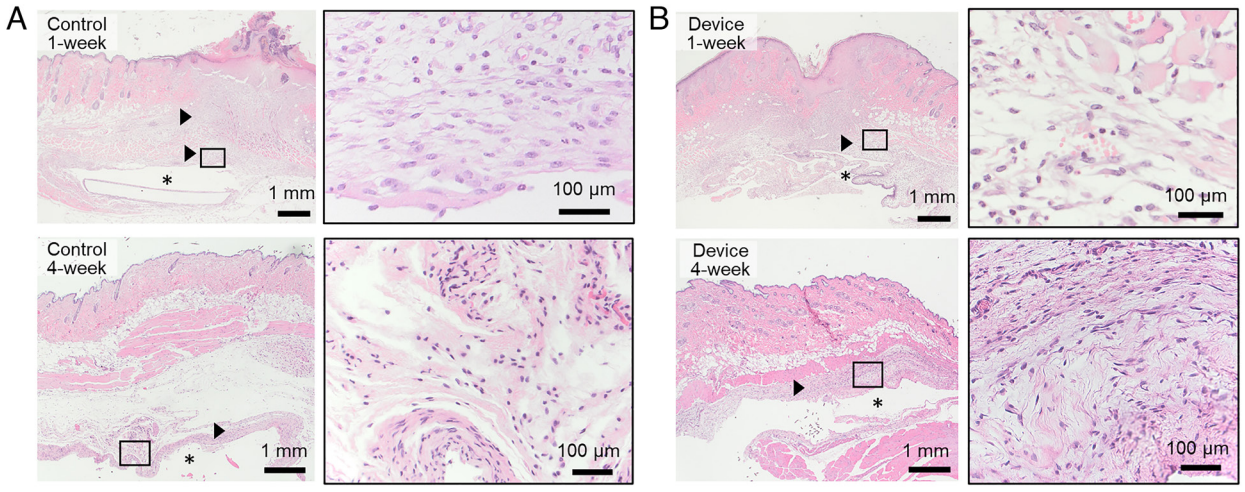

Fig. 6. Histological studies of control and full devices. (*A* and *B*) Representative images of H&E stained cross-sectional areas near the implantation site of control (*A*) and device (*B*) groups at the 1-wk and 4-wk endpoints. n = 4 biologically independent animals. Subcutaneous cavitation corresponds to the device implantation site (asterisk). Loose infiltrates of mixed inflammatory cells are present in the dermal and subcutaneous tissues (arrowheads). Inflammatory cells in the subcutaneous tissue consist of a mixture of histiocytes, neutrophils, and fibroblasts (*Inset*, square).

suggests an ability to independently control no more than 30 reservoirs. Spatial selectivity in illumination might provide a route to further increase the number of reservoirs. Adapted versions of the platforms reported here also have potential for chronic treatments and cocktail therapies, as additional areas for future work.

Materials and Methods

Fabrication of Transient Batteries. An ultraviolet laser prototyping system (LPKF U4) defined the shapes of the anodes and cathodes from foils of Mg (50 or 100 μm, Alibaba), Zn (10 or 20 μm, Alibaba), Mo (5 or 50 μm, Alibaba), and W (50 μm, Alibaba) and from foils of Fe (3 or 25 μm, Alfa Aesar). Mg-Fe, Mg-Mo, and Mg-W batteries incorporated anodes of Mg, cathodes of Fe, Mo, or W, and electrolytes of phosphate buffered solution (PBS, Sigma-Aldrich). Mg-MoO_3 and Zn-MoO_3 batteries combined anodes of Mg or Zn with MoO_3 cathodes, respectively, in PBS electrolytes. Mixing 0.45 g MoO_3 (Sigma Aldrich), 0.05 g carbon black, and 800 μL of 300 mg/mL poly (D,L-lactide-co-glycolide) (PLGA, lactide/glycolide 65:35, M_w 40 to 75k, Sigma-Aldrich) in ethyl acetate within a planetary mixer (Thinky ARE-30) yielded a slurry for the MoO_3 cathode. Mo gauze (40 mesh, Alfa Aesar) and Mo foil (5 or 50 μm) served as current collectors for the cathode materials. Applying the slurries on these current collectors and baking at 65 °C for 30 min completed the process.

Electrochemical Measurements. Methods for discharging the transient batteries used two different conditions 1) constant current discharge (CCD) at 0.4 mA cm_{Anode}^{-2} using the chronopotentiometry technique, and 2) constant voltage discharge (CVD) at 0 V using the chronoamperometry technique. Linear sweep voltammetry (LSV) and electrochemical impedance spectroscopy (EIS) measurements involved a three-electrode setup in PBS with Mg or Mg-SOG as the working electrode, Pt wire as the counter electrode, and Ag/AgCl as the reference electrode. For LSV, the scanning potential ranged from −250 mV to 250 mV at a rate of 1 mV/s. EIS under galvanostatic mode used a frequency range of 10 kHz to 0.1 Hz, with a current amplitude of 0.1 μA. All electrochemical measurements relied on a PalmSens4 system.

Forming Coatings of Spin-on-Glass (SOG) and SiO_2 on Mg Foils. Spin casting (1,000 rpm for 10 s) a polysiloxane-based spin-on dielectric material (IC1-200, Futurrex) on Mg foils, followed by baking at 250 °C for 2 h, yielded coating of SOG with thicknesses of ~500 nm (Mg-SOG). Repeating this process formed coatings on both sides of the foils. Forming films of SiO_2 with thicknesses of 100 nm and 1 μm by sputter deposition onto Mg foils yielded SiO_2-coated Mg foils (Mg-SiO_2).

Material Characterization. Morphological and compositional analyses used scanning electron microscopy (SEM, Hitachi SU 8030). A Thermo Scientific ESCALAB QXi XPS Microprobe-enabled X-ray photoelectron spectroscopy (XPS) measurements. Fourier transform infrared spectroscopy (FTIR) used a Nexus 870 spectrometer. A Filmetrics F20 instrument yielded the thicknesses of the layers of SOG. A Keyence microscope captured all optical micrographs.

Fabrication of Drug Delivery Devices. Polybutanedithiol 1,3,5-triallyl-1,3,5-triazine-2,4,6(1*H*,3*H*,5*H*)-trione pentanoic anhydride (PA) (29) served as the material for the drug reservoirs (total size of 19 mm × 13 mm × 1.25 mm for three reservoirs), synthesized through thiol-ene click reactions of three compounds: 4-pentenoic anhydride (4PA, Sigma-Aldrich), 1,3,5-triallyl-1,3,5-triazine-2,4,6(1H,3H,5H)-trione (TTT, Sigma-Aldrich), and 1,4-butanedithiol (Sigma-Aldrich). 4-PA, TTT, and 1,4-butanedithiol mixed with a molar ratio of 1:1:2.5 (for accelerated aging test) or 1:4:7 (for all other experiments) in Ecoflex 35 molds, followed by exposure to ultraviolet (UV, wavelength of 365 nm) light with 2,2-dimethoxy-2-phenylacetophenone (Sigma-Aldrich) as the photoinitiator (total mass of 0.5%). Disks of 5 mm × 5 mm Mg (20 to 50 μm, wet-etched), Mg-SOG (20 to 50 μm), and Zn (20 μm) defined by a laser cutting process served as the metal gates. Laser-cut 5 mm × 17 mm Mo and Fe foils served as cathodes. A flat film of PA (19 mm × 13 mm × 0.25 mm) sealed the reservoirs. Extended metal electrodes connected to a commercial phototransistor (Digi-Key, NTE3120A). Optical filters (Edmund Optics) placed atop the phototransistors provided a wavelength-selective response. Biodegradable conductive paste (Candelilla wax/W powder) (30) electrically connected the individual components. Three sets of optical filters and light-emitting diodes (Digi-Key) enabled programmable release of drugs from the reservoirs. A digital multimeter measured the resistance of a phototransistor placed underneath each optical filter and illuminated by each LED.

Finite Element Analysis. 3D FEA used the commercial software Ansys Maxwell to define the distributions of current density associated with the drug release devices. The use of an adaptive mesh (tetrahedron elements) ensured computational accuracy. The relative permittivity (ε_r) and bulk conductivity (σ) were 80 and 1.4 $S{\cdot}m^{-1}$ for PBS, and 3 and $6.7{*}10^{-16}$ S m^{-1} for PA. The electromagnetic parameters of other materials relied on the material library in the Ansys Maxwell software package.

Measurements of Cumulative Release of Drug. Tests involved a single drug reservoir with gates of Mg, Mg-SOG, or Zn and filled with 0.005 M Rhodamine B solution, triggered to release this solution into surrounding PBS or incubated at 37 °C in PBS to investigate the release process through different gates. At regular time intervals, 3 mL of surrounding PBS was drawn from the vial for UV–VIS spectroscopic analysis (HP8452, Agilent Technologies), subsequently returned to the vial after each measurement. The concentration of Rhodamine B followed from measurements of the absorption peak at 554 nm.

In Vivo Demonstration of Programmable Lidocaine Release for Sciatic Nerve Block. Drug delivery devices with three drug reservoirs filled with lidocaine (Xylocaine-HCL 2%, Astra Zeneca Pharma) were surgically implanted onto

the right sciatic nerves of female Sprague–Dawley rats (200 to 250 g, Charles River Laboratories). All animal procedures were performed in accordance with the ethical standards and protocols of Northwestern University. During implantation, rats were anesthetized using isoflurane gas (3% for induction and 1 to 2% for maintenance). After the implantation, the muscle was closed with 6-0 Vicryl sutures and the skin incision was closed with Autoclip wound clips (12020-09, Fine Science Tools). Three LEDs placed over the implantation site served as the basis for programmable triggering of the release of lidocaine from anyone or any arbitrary combination of reservoirs. CMAP and SNAP were measured with 1″ length, 0.25-mm diameter concentric needle electrodes (UTC-25F, The Electrode Store) on a VikingQuest EMG system using Synergy master software (Natus). (Data are means ± SD; n = 3.) To confirm the physiological effect of the lidocaine being released, devices (filled with ~230 μL lidocaine) were implanted adjacent to the right sciatic nerves of rats followed by triggering the drug release process under anesthesia. After 30 min, these rats completely woke up. Hindlimb strength measurements were made with a digital grip strength meter with mesh assembly (Columbus Instruments, Columbus, OH) with the average of 3 to 5 trials recorded. Nociception function was assessed by recording the paw's withdrawal threshold from mechanical stimulation using an electronic Von Frey system (Harvard Apparatus, Holliston, Massachusetts) with the average of 3 to 5 trials recorded.

In Vitro Cytocompatibility. In vitro cytocompatibility studies of the device against human cells (Normal human dermal fibroblasts, NHDF, CC-2511, Lonza) were performed through both direct and indirect contact methods. A mixture of fibroblast basal medium (ATCC, CAT# PCS-201-030), 10 vol.% fetal bovine serum (Thermo Fisher Scientific) and 1 vol.% penicillin–streptomycin (Thermo Fisher Scientific) served as the cell culture medium. In direct contact experiments, samples were incubated in the cell-seeded wells for 24 h. In indirect contact experiments, incubating samples in cell medium for 24 h resulted sample extracts (ISO 10993-12), which were centrifuged at 14,000 rpm for 10 min. Supernatants were added into the cell-seeded wells for 24 h. Cells stained with a live/dead viability/cytotoxicity kit (L3224; Thermo Fisher Scientific) according to the manufacturer's protocols allowed the quantitative evaluations of the cytocompatibility of samples, including control (PA) and device groups.

In Vivo Biocompatibility Tests. All procedures were performed in accordance with the ethical standards and protocols of Northwestern University. Each male CD-1 mouse (33 to 38 g) was placed under isoflurane anesthesia (~3%), then given pre-operative analgesia (SQ: 20 mg/kg Meloxicam, line block of 2 mg/kg - 0.1% Bupivacaine). Under sterile conditions, a ~0.7-cm incision was made on the back. Two types of devices (PA-Mg-SOG, n = 4, and PA-Mg-SOG-Fe, n = 4) and a control group (PA, n = 4) were implanted subcutaneously in the interscapular region. In group PA-Mg-SOG-Fe, Mg, and Fe were electrically connected by biodegradable conductive W paste. Mice were weighed and checked at regular time intervals. Blood, skin, muscle adjacent to the device, and organs (brain, heart, lung, liver, spleen, and kidney) were collected at 1- and 4-wk endpoints. Skin, muscle, and organ tissues were fixed in 10% neutral-buffered formalin, embedded in paraffin, and stained with hematoxylin and eosin (H&E) for histological analysis. Concentrations of Mg, Si, and Fe in the organs were measured by inductively coupled plasma optical emission spectrometry (ICP-OES).

Histological Scoring. The histologic evaluation of the tissue was performed and a five-grade scoring system was used to record the histopathology severity. Each H&E slide was carefully reviewed for the presence of fibrosis, mesenchymal cells, hematopoietic cells, basophilia and inflammation. Severity was scored as 0 = none, 1 = minimal, 2 = mild, 3 = moderate, 4 = marked, and 5 = severe.

Data, Materials, and Software Availability. All study data are included in the article and/or *SI Appendix*.

ACKNOWLEDGMENTS. This work was supported by the Querrey Simpson Institute for Bioelectronics. We specially thank Quanhong Ma, Nayereh Ghoreishi-Haack, Iwona Stepien, Shuling Han, and Chad Haney for the help in the biocompatibility study, animal experiment, and imaging. This work made use of the Northwestern University Micro/Nano Fabrication Facility of Northwestern University's Atomic and Nanoscale Characterization Experimental Center, which has received support from the Soft and Hybrid Nanotechnology Experimental Resource (NSF ECCS-2025633), the International Institute for Nanotechnology, and Northwestern University Materials Research Science and Engineering Center program (NSF DMR-1720139). This work was supported by the Developmental Therapeutics Core at Northwestern University and the Robert H. Lurie Comprehensive Cancer Center support grant (NCI P30 CA060553). C.K.F. would like to acknowledge support from the Belle Carnell Regenerative Neurorehabilitation fund.

Author affiliations: [a]Center for Bio-Integrated Electronics, Northwestern University, Evanston, IL 60208; [b]Querrey Simpson Institute for Bioelectronics, Northwestern University, Evanston, IL 60208; [c]Department of Materials Science and Engineering, Northwestern University, Evanston, IL 60208; [d]Regenerative Neurorehabilitation Laboratory, Shirley Ryan Ability Lab, Chicago, IL 60611; [e]Department of Mechanical Engineering, Northwestern University, Evanston, IL 60208; [f]Department of Electronic Engineering, Gachon University, Seongnam-si, Gyeonggi-do 13120, Republic of Korea; [g]Department of Neurobiology, Northwestern University, Evanston, IL 60208; [h]Department of Chemical and Biological Engineering, Northwestern University, Evanston, IL 60208; [i]Department of Chemical Engineering, Dankook University, Yongin 16890, Republic of Korea; [j]Charles River Laboratories, Mattawan, MI 49071; [k]Developmental Therapeutics Core, Northwestern University, Evanston, IL 60208; [l]Department of Biomedical Engineering, Northwestern University, Evanston, IL 60208; [m]Department of Physical Medicine and Rehabilitation, Feinberg School of Medicine, Northwestern University, Chicago, IL 60611; [n]The Ken and Ruth Davee Department of Neurology, Feinberg School of Medicine, Northwestern University, Chicago, IL 60611; and [o]Department of Neurological Surgery, Feinberg School of Medicine, Northwestern University, Chicago, IL 60611

Author contributions: Yamin Zhang, C.K.F., and J.A.R. designed research; Yamin Zhang, F.L., Yuhe Zhang, J.W., D.D., J.B.W., Shupeng Li, M.W., Shuo Li, Z.H., T.W., J.C., E.D., K.Z., A.L., Y.B., I.H., H.G., X.N., Y.W., G.L., and F.J. performed research; Yamin Zhang and H.-J.Y. contributed new reagents/analytic tools; Yamin Zhang, F.L., Yuhe Zhang, K.B., Y.H., C.K.F., and J.A.R. analyzed data; and Yamin Zhang, C.K.F., and J.A.R. wrote the paper.

1. M. A. Luzuriaga, D. R. Berry, J. C. Reagan, R. A. Smaldone, J. J. Gassensmith, Biodegradable 3D printed polymer microneedles for transdermal drug delivery. *Lab Chip* **18**, 1223–1230 (2018).
2. S. Y. Chin *et al.*, Additive manufacturing of hydrogel-based materials for next-generation implantable medical devices. *Sci. Robot.* **2**, eaah6451 (2017).
3. I. S. Tobias *et al.*, Zero-order controlled release of ciprofloxacin-HCl from a reservoir-based, bioresorbable and elastomeric device. *J. Control. Release* **146**, 356–362 (2010).
4. C. J. Bettinger, Synthetic biodegradable elastomers for drug delivery and tissue engineering. *Pure Appl. Chem.* **83**, 9–24 (2010).
5. M. L. Macdonald *et al.*, Tissue integration of growth factor-eluting layer-by-layer polyelectrolyte multilayer coated implants. *Biomaterials* **32**, 1446–1453 (2011).
6. Q. Yao, Y. Liu, B. Selvaratnam, R. T. Koodali, H. Sun, Mesoporous silicate nanoparticles/3D nanofibrous scaffold-mediated dual-drug delivery for bone tissue engineering. *J. Control. Release* **279**, 69–78 (2018).
7. X. Zhao *et al.*, Active scaffolds for on-demand drug and cell delivery. *Proc. Natl. Acad. Sci. U.S.A.* **108**, 67–72 (2011).
8. Y. Qiu *et al.*, Magnetic forces enable controlled drug delivery by disrupting endothelial cell-cell junctions. *Nat. Commun.* **8**, 15594 (2017).
9. R. Farra *et al.*, First-in-human testing of a wirelessly controlled drug delivery microchip. *Sci. Transl. Med.* **4**, 1–11 (2012).
10. M. Staples, K. Daniel, M. J. Cima, R. Langer, Application of micro- and nano-electromechanical devices to drug delivery. *Pharm. Res.* **23**, 847–863 (2006).
11. Y. Zhang *et al.*, Battery-free, lightweight, injectable microsystem for in vivo wireless pharmacology and optogenetics. *Proc. Natl. Acad. Sci. U.S.A.* **116**, 21427–21437 (2019).
12. C. H. Lee *et al.*, Biological lipid membranes for on-demand, wireless drug delivery from thin, bioresorbable electronic implants. *NPG Asia Mater.* **7**, e227–e227 (2015).
13. J. Lee *et al.*, Flexible, sticky, and biodegradable wireless device for drug delivery to brain tumors. *Nat. Commun.* **10**, 5205 (2019).
14. S. Dromi *et al.*, Pulsed-high intensity focused ultrasound and low temperature-sensitive liposomes for enhanced targeted drug delivery and antitumor effect. *Clin. Cancer Res.* **13**, 2722–2727 (2007).
15. J. Koo *et al.*, Wirelessly controlled, bioresorbable drug delivery device with active valves that exploit electrochemically triggered crevice corrosion. *Sci. Adv.* **6**, eabb1093 (2020).
16. C. R. Thomas *et al.*, Noninvasive remote-controlled release of drug molecules in vitro using magnetic actuation of mechanized nanoparticles. *J. Am. Chem. Soc.* **132**, 10623–10625 (2010).
17. D. P. Ferris *et al.*, Light-operated mechanized nanoparticles. *J. Am. Chem. Soc.* **131**, 1686–1688 (2009).
18. S. M. Mirvakili, R. Langer, Wireless on-demand drug delivery. *Nat. Electron.* **4**, 464–477 (2021).
19. W. Gao *et al.*, Cargo-towing fuel-free magnetic nanoswimmers for targeted drug delivery. *Small* **8**, 460–467 (2012).
20. W. Gao, J. Wang, Synthetic micro/nanomotors in drug delivery. *Nanoscale* **6**, 10486–10494 (2014).
21. C. M. Proctor *et al.*, An electrocorticography device with an integrated microfluidic ion pump for simultaneous neural recording and electrophoretic drug delivery in vivo. *Adv. Biosyst.* **3**, 1800270 (2019).
22. S. Chen *et al.*, Reducing passive drug diffusion from electrophoretic drug delivery devices through co-ion engineering. *Adv. Sci.* **8**, 2003995 (2021).
23. J. T. Santini, M. J. Cima, R. Langer, A controlled-release microchip. *Nature* **397**, 335–338 (1999).
24. P. Nadeau *et al.*, Prolonged energy harvesting for ingestible devices. *Nat. Biomed. Eng.* **1**, 0022 (2017).
25. I. Huang *et al.*, High performance dual-electrolyte magnesium-iodine batteries that can harmlessly resorb in the environment or in the body. *Energy Environ. Sci.* **15**, 4095–4108 (2022).
26. L. Yin *et al.*, Dissolvable metals for transient electronics. *Adv. Funct. Mater.* **24**, 645–658 (2014).

27. X. Huang *et al.*, A fully biodegradable battery for self-powered transient implants. *Small* **14**, 1800994 (2018).
28. L. Yin *et al.*, Materials, designs, and operational characteristics for fully biodegradable primary batteries. *Adv. Mater.* **26**, 3879–3884 (2014).
29. Y. S. Choi *et al.*, Biodegradable polyanhydrides as encapsulation layers for transient electronics. *Adv. Funct. Mater.* **30**, 2000941 (2020).
30. J. Koo *et al.*, Wireless bioresorbable electronic system enables sustained nonpharmacological neuroregenerative therapy. *Nat. Med.* **24**, 1830–1836 (2018).
31. W. F. Ng, K. Y. Chiu, F. T. Cheng, Effect of pH on the in vitro corrosion rate of magnesium degradable implant material. *Mater. Sci. Eng. C* **30**, 898–903 (2010).
32. Y. Qi, X. Li, Y. He, D. Zhang, J. Ding, Mechanism of acceleration of iron corrosion by a polylactide coating. *ACS Appl. Mater. Interfaces* **11**, 202–218 (2019).
33. W. A. Badawy, F. M. Al-Kharafi, Corrosion and passivation behaviors of molybdenum in aqueous solutions of different pH. *Electrochim. Acta* **44**, 693–702 (1998).
34. S.-K. Kang *et al.*, Dissolution behaviors and applications of silicon oxides and nitrides in transient electronics. *Adv. Funct. Mater.* **24**, 4427–4434 (2014).
35. Y. Zhang *et al.*, The effect of enzymes on the in vitro degradation behavior of Mg alloy wires in simulated gastric fluid and intestinal fluid. *Bioact. Mater.* **7**, 217–226 (2022).
36. A. Göpferich, J. Tessmar, Polyanhydride degradation and erosion. *Adv. Drug Deliv. Rev.* **54**, 911–931 (2002).
37. A. J. Domb, R. Nudelman, In vivo and in vitro elimination of aliphatic polyanhydrides. *Biomaterials* **16**, 319–323 (1995).
38. Y. Gao *et al.*, Effect of stress on corrosion of high-purity magnesium in vitro and in vivo. *Acta Biomater.* **83**, 477–486 (2019).
39. A. Tamayo *et al.*, Mesoporous silicon oxycarbide materials for controlled drug delivery systems. *Chem. Eng. J.* **280**, 165–174 (2015).
40. G. Song, Control of biodegradation of biocompatable magnesium alloys. *Corros. Sci.* **49**, 1696–1701 (2007).
41. Q. He, J. Shi, M. Zhu, Y. Chen, F. Chen, The three-stage in vitro degradation behavior of mesoporous silica in simulated body fluid. *Microporous Mesoporous Mater.* **131**, 314–320 (2010).
42. A. Schauer *et al.*, Biocompatibility and degradation behavior of molybdenum in an in vivo rat model. *Materials* **14**, 7776 (2021).
43. J. Kuhlmann *et al.*, Fast escape of hydrogen from gas cavities around corroding magnesium implants. *Acta Biomater.* **9**, 8714–8721 (2013).
44. A. Gangan *et al.*, Influence of pH values on the electrochemical performance of low carbon steel coated by plasma thin SiOxCy films. *Arab. J. Chem.* **14**, 103391 (2021).
45. M. Arango-Ospina *et al.*, Review: Silicon oxycarbide based materials for biomedical applications. *Appl. Mater. Today* **18**, 100482 (2020).
46. J. D. Romero, M. Khan, H. Fatemi, J. Turlo, Outgassing behavior of spin-on-glass (SOG). *J. Mater. Res.* **6**, 1996–2003 (1991).
47. C. Paluszkiewicz, T. Gumuła, J. Podporska, M. Błażewicz, Structure and bioactivity studies of new polysiloxane-derived materials for orthopedic applications. *J. Mol. Struct.* **792–793**, 176–181 (2006).
48. T. Gumula, C. Paluszkiewicz, M. Blazewicz, Structural characterization of polysiloxane-derived phases produced during heat treatment. *J. Mol. Struct.* **704**, 259–262 (2004).
49. A. Francis, R. Detsch, A. R. Boccaccini, Fabrication and cytotoxicity assessment of novel polysiloxane/bioactive glass films for biomedical applications. *Ceram. Int.* **42**, 15442–15448 (2016).
50. J. Liang, P. B. Srinivasan, C. Blawert, W. Dietzel, Influence of chloride ion concentration on the electrochemical corrosion behaviour of plasma electrolytic oxidation coated AM50 magnesium alloy. *Electrochim. Acta* **55**, 6802–6811 (2010).
51. I. Oshina, J. Spigulis, Beer-Lambert law for optical tissue diagnostics: Current state of the art and the main limitations. *J. Biomed. Opt.* **26**, 100901 (2021).
52. S.-H. Tseng, P. Bargo, A. Durkin, N. Kollias, Chromophore concentrations, absorption and scattering properties of human skin in-vivo. *Opt. Express* **17**, 14599 (2009).
53. H. Jonasson *et al.*, In vivo characterization of light scattering properties of human skin in the 475- to 850-nm wavelength range in a Swedish cohort. *J. Biomed. Opt.* **23**, 1 (2018).
54. I. L. Rosenfeld, I. K. Marshakov, Mechanism of crevice corrosion. *Corrosion* **20**, 115t–125t (1964).
55. J. G. Thalhammer, M. Vladimirova, B. Bershadsky, G. R. Strichartz, Neurologic evaluation of the rat during sciatic nerve block with lidocaine. *Anesthesiology* **82**, 1013–1025 (1995).
56. N. Waegeneers *et al.*, Short-term biodistribution and clearance of intravenously administered silica nanoparticles. *Toxicol. Rep.* **5**, 632–638 (2018).
57. G. Bortolussi *et al.*, Long-term effects of biliverdin reductase a deficiency in Ugt1−/− mice: Impact on redox status and metabolism. *Antioxidants* **10**, 2029 (2021).
58. M. F. Cesta, Normal structure, function, and histology of the spleen. *Toxicol. Pathol.* **34**, 455–465 (2006).
59. H. Xiao *et al.*, Antineutrophil cytoplasmic autoantibodies specific for myeloperoxidase cause glomerulonephritis and vasculitis in mice. *J. Clin. Invest.* **110**, 955–963 (2002).
60. D. G. Barone *et al.*, Prevention of the foreign body response to implantable medical devices by inflammasome inhibition. *Proc. Natl. Acad. Sci. U.S.A.* **119**, e2115857119 (2022).
61. W. Bai *et al.*, Bioresorbable photonic devices for the spectroscopic characterization of physiological status and neural activity. *Nat. Biomed. Eng.* **3**, 644–654 (2019).
62. D. Zhao *et al.*, In vivo characterization of magnesium alloy biodegradation using electrochemical H2 monitoring, ICP-MS, and XPS. *Acta Biomater.* **50**, 556–565 (2017).
63. L. Yang *et al.*, Size dependent biodistribution and toxicokinetics of iron oxide magnetic nanoparticles in mice. *Nanoscale* **7**, 625–636 (2015).
64. V. R. Shrestha, S.-S. Lee, E.-S. Kim, D.-Y. Choi, Non-iridescent transmissive structural color filter featuring highly efficient transmission and high excitation purity. *Sci. Rep.* **4**, 4921 (2014).